The Transient Response of the Southern Ocean to Stratospheric Ozone Depletion

WILLIAM J. M. SEVIOUR, ANAND GNANADESIKAN, AND DARRYN W. WAUGH

Department of Earth and Planetary Sciences, Johns Hopkins University, Baltimore, Maryland

(Manuscript received 7 March 2016, in final form 2 June 2016)

ABSTRACT

Recent studies have suggested that the response of the Southern Ocean to stratospheric ozone depletion is nonmonotonic in time; consisting of an initial cooling followed by a long-term warming. This result may be significant for the attribution of observed Southern Ocean temperature and sea ice trends, but the time scale and magnitude of the response is poorly constrained, with a wide spread among climate models. Furthermore, a long-lived initial cooling period has only been observed in a model with idealized geometry and lacking an explicit representation of ozone. Here the authors calculate the transient response of the Southern Ocean to a step-change in ozone in a comprehensive coupled climate model, GFDL-ESM2Mc. The Southern Ocean responds to ozone depletion with an initial cooling, lasting 25 yr, followed by a warming. The authors extend previous studies to investigate the dependence of the response on the ozone forcing as well as the regional pattern of this response. The response of the Southern Ocean relative to natural variability is shown to be largely independent of the initial state. However, the magnitude of this response is much less than that of natural variability found in the model, which limits its influence and detectability.

1. Introduction

In recent decades significant trends in the summertime atmospheric circulation over the Southern Ocean (SO) have been observed. The extratropical jet has shifted poleward and intensified (Thompson et al. 2011; Swart and Fyfe 2012; Hande et al. 2012), consistent with a more positive southern annular mode (SAM). These trends are outside the range of natural variability found in coupled climate models (Thomas et al. 2015) and have been largely attributed to the impact of stratospheric ozone depletion (Polvani et al. 2011; Gerber and Son 2014). At the same time, an increase in Southern Hemisphere sea ice cover has been observed (Comiso and Nishio 2008; Parkinson and Cavalieri 2012), most prominent in the fall and in contrast to the large decrease seen in the Arctic.

Several studies have investigated a possible link between these atmospheric and ocean–sea ice trends. The sea surface temperature (SST) pattern associated with interannual variability in the SAM is a dipole in the meridional direction, a feature driven largely by horizontal Ekman transport (as well as vertical Ekman pumping in summer; Purich et al. 2016), and is consistent across observations and climate models (Watterson 2000; Hall and Visbeck 2002; Sen Gupta and England 2006; Ciasto and Thompson 2008). For the positive phase of the SAM, this pattern gives a warming in SST at about 40°S and cooling south of about 50°S, leading to an overall increase in SO sea ice cover (Lefebvre et al. 2004; Lefebvre and Goosse 2008; Purich et al. 2016). Following these results, Goosse et al. (2009) argued that the ozone-driven trend toward a more positive SAM is the main driver of the observed SO sea ice expansion. However, this contradicts the results of many coupled climate model studies that have found a warming of the SO and a reduction in sea ice extent associated with stratospheric ozone depletion (Sigmond and Fyfe 2010; Bitz and Polvani 2012; Smith et al. 2012; Sigmond and Fyfe 2014; Previdi et al. 2014; Solomon et al. 2015a).

Ferreira et al. (2015, hereafter F15) attempted to reconcile these opposing views by proposing that the response of the SO to stratospheric ozone depletion has two time scales: a fast and slow response. They found the fast response to be similar to the interannual SAM–SST correlation, driven by horizontal Ekman transport, and leading to an increase in sea ice cover. On the other hand, the slow response was shown to be driven by upwelling of warm water from below the mixed layer,

Corresponding author address: William Seviour, Department of Earth and Planetary Sciences, Johns Hopkins University, 3400 N. Charles St., Baltimore, MD 21218.
E-mail: wseviou1@jhu.edu

DOI: 10.1175/JCLI-D-16-0198.1

leading to a reduction in sea ice cover, consistent with coupled climate modeling studies. F15 computed the transient ocean response to a step function in ozone depletion in two coupled climate models: the MITgcm and CCSM3.5. These two simulations had very different configurations, with the MITgcm using an idealized geometry (Double Drake) and without an explicit representation of ozone, while CCSM3.5 is a more comprehensive coupled model with explicit ozone, realistic geometry, and more sophisticated radiation and cloud schemes. While F15 showed both models to give a two-time-scale response, there were also significant differences between the simulations. The initial cooling period was about 20 yr in the MITgcm but just 5 yr in CCSM3.5. Furthermore, the magnitude of the cooling was around 3 times greater in the MITgcm than CCSM3.5.

More recently, Kostov et al. (2016) investigated the response of the SO to a step increase in the SAM by studying lagged correlations in preindustrial control simulations included in phase 5 of the Coupled Model Intercomparison Project (CMIP5). They found a wide range of responses, with some models giving a two-time-scale response but others with persistent cooling. Among those models that did show a two-time-scale response there was a wide range of times at which SST anomalies cross from negative to positive. Better constraining the time scales and magnitudes of this response will be crucial in determining how much (if any) of the observed sea ice trends may be attributed to ozone depletion, as well as how ozone recovery may influence future SO changes.

In this study, we calculate the transient response of the Southern Ocean to stratospheric ozone depletion in the Geophysical Fluid Dynamics Laboratory Earth System Model with Modular Ocean Model (GFDL-ESM2Mc) coupled climate model. Specifically, we study the response to a step change in stratospheric ozone depletion, a similar approach to F15, described in general terms by Marshall et al. (2014). An advantage of calculating this response is that linear theory allows the step function response to be used to predict the response to an arbitrary time-varying forcing. This approach also allows the mechanisms driving the response to ozone forcing to be more clearly isolated than if the forcing itself is time-varying. We find an initial cooling lasting about 25 yr, followed by a warming, and a similar magnitude found by F15 for the MITgcm. This demonstrates that a long-lived cooling such as that found for the MITgcm is possible in a climate model with realistic geometry and explicitly represented ozone. However, this response is small relative to the natural variability of the model and only clearly emerges in an ensemble of simulations. We extend F15 to investigate how the response depends on the prescribed ozone forcing and the initial conditions. We also investigate the spatial structure of the response, showing that both the time scales and magnitudes of the response vary over the SO.

2. Ozone response simulations

The GFDL-ESM2Mc model (Gnanadesikan et al. 2015) used here is a coarse-resolution version of GFDL-ESM2M (Galbraith et al. 2011; Dunne et al. 2012). The model consists of a 3.875° × 3° latitude–longitude atmosphere with 24 vertical levels, coupled to a 3° × 1.5° ocean model with 28 vertical levels. In the ocean model, advection due to geostrophic eddies is parameterized using a spatially varying mixing coefficient A_{GM} (Gent and McWilliams 1990), which depends on the horizontal shear between 100 and 2000 m. A minimum coefficient of 200 $m^2 s^{-1}$ and a maximum coefficient of 1400 $m^2 s^{-1}$ are imposed, and the slope-dependent thickness transport also stops increasing at a value of 0.01 A_{GM} to prevent unrealistically large velocities near mixed layers where slopes become infinite. A lateral eddy mixing coefficient A_{Redi} (Redi 1982) with a global value of 800 $m^2 s^{-1}$ is also included. A nonlocal K-profile parameterization scheme (Large et al. 1994) is used for vertical mixing within the ocean boundary layer, and a vertical diffusivity of 1×10^{-5} $m^2 s^{-1}$ is specified within the ocean interior. Within the mixed layer the model also uses the parameterization for mixed layer restratification developed by Fox-Kemper et al. (2008). This parameterization produces an overturning circulation that increases with the mixed layer depth, the magnitude of the lateral density gradient within the layer, and the radius of deformation.

Initial conditions for our simulations are taken from a 500-yr-long preindustrial control simulation using a global carbon dioxide concentration of 286 ppm and ozone concentrations for the year 1860 from the stratosphere–troposphere processes and their role in climate (SPARC) dataset (Cionni et al. 2011). The zonal mean wind stress in this control simulation has a maximum of 0.15 Pa at the grid point centered at 49.5S. If instead the maximum is computed at each longitude and averaged across the basin, the average latitude is found at 50.3°S. The maximum wind stress is essentially identical to the value found in the ensemble coupled data assimilation product (Zhang et al. 2007) as well as the values reported by Large and Yeager (2009). The Antarctic Circumpolar Current in the model has a transport of 164 Sv (1 Sv ≡ 10^6 $m^3 s^{-1}$) through Drake Passage, which is on the high end of the range of observational estimates (Meijers et al. 2012). In combination, the wind stress and transport characteristics of the model make it

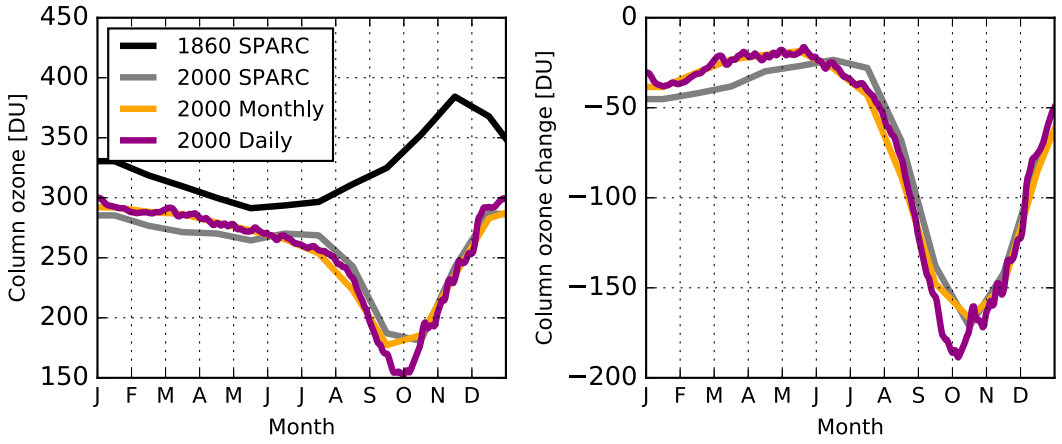

FIG. 1. (left) Seasonal cycle of polar cap (70°–90°S) averaged column ozone in the control simulation (1860 SPARC) and the perturbation simulations with year-2000 ozone prescribed with monthly and daily mean values from WACCM-SD. (right) Difference of 2000 ozone and 1860 ozone simulations. Also shown for comparison is 2000 column ozone from the SPARC dataset and the difference between 2000 and 1860 SPARC values (gray line).

relatively competitive with the 23 models studied by Meijers et al. (2012). As noted by Galbraith et al. (2011), the model has a relatively realistic representation of the southern annular mode. The main biases in GFDL-ESM2Mc, in common with other members of the GFDL CM2.0 suite (Dunne et al. 2012), stem from a tendency toward too little cloudiness during the Antarctic summer. This leads to a warm bias in SST and a low bias in sea ice; in the control model sea ice essentially vanishes during the Antarctic summer (Pradal and Gnanadesikan 2014). During the winter, however, Antarctic sea ice in our model covers an area of 15.7×10^6 km^2, closer to observations than many other models in the CMIP5 series (Turner et al. 2013).

From this control simulation further simulations are branched in which we instantaneously impose a change to contemporary ozone concentrations, using a zonal-mean climatology from 1995–2001. These contemporary concentrations are derived from a specified dynamics version of the Whole Atmosphere Community Climate Model (WACCM-SD), in which temperatures and winds are nudged to meteorological assimilation analysis results but chemistry is calculated interactively (Solomon et al. 2015b). Neely et al. (2014) have proposed that the coarse temporal resolution (monthly mean) of prescribed ozone used by many simulations leads to an underestimate of the magnitude of ozone depletion. To test this, we impose daily mean concentrations in half of the simulations and monthly means of these daily values in the other half. The seasonal cycles of polar cap (70°–90°N) column ozone for these imposed ozone concentrations are shown in Fig. 1. Ozone is reduced relative to preindustrial concentrations throughout the year, but the largest difference between monthly and daily values is seen to occur in the spring (September–November), and the minimum around 1 October is less pronounced for the monthly mean ozone than daily mean because of the linear interpolation used. The monthly mean ozone changes imposed here are similar to those of the SPARC dataset, although with slightly less depletion during the summer and spring (Fig. 1).

The SO in GFDL-ESM2Mc displays significant multidecadal variability, a feature seen in several, but not all, coupled climate models (de Lavergne et al. 2014; Martin et al. 2013). Figure 2 shows the time series of SO SST for 200 yr of the preindustrial control simulation. Multidecadal variability is apparent, with a period of approximately 50 yr, and this variability is dominated by the Ross and Weddell Seas (Fig. 2b). Variability in these two regions is correlated but largest in the Weddell Sea, which shows the most extreme minima and maxima. Further investigation shows this variability to be predominantly caused by large deep convective events in these regions, as was previously reported by Galbraith et al. (2011) in a similar model. We test the dependence of the SO response to ozone depletion on the initial conditions by initializing half of the ozone response simulations with relatively cold SO SST ("cold start") and half relatively warm ("warm start"), as illustrated in Fig. 2a. These initialization dates are clustered around two warm and cold periods and spaced 5 yr apart within each period. Testing the dependence of this response on initial conditions is particularly important because the ability to reconstruct the response to an arbitrary forcing from the step function response relies on linear theory. A necessary condition of the response being linear is that it is independent of the initial conditions.

In total, we run 24 ozone response simulations, each 48 yr long. These are divided into 12 start dates (6 warm

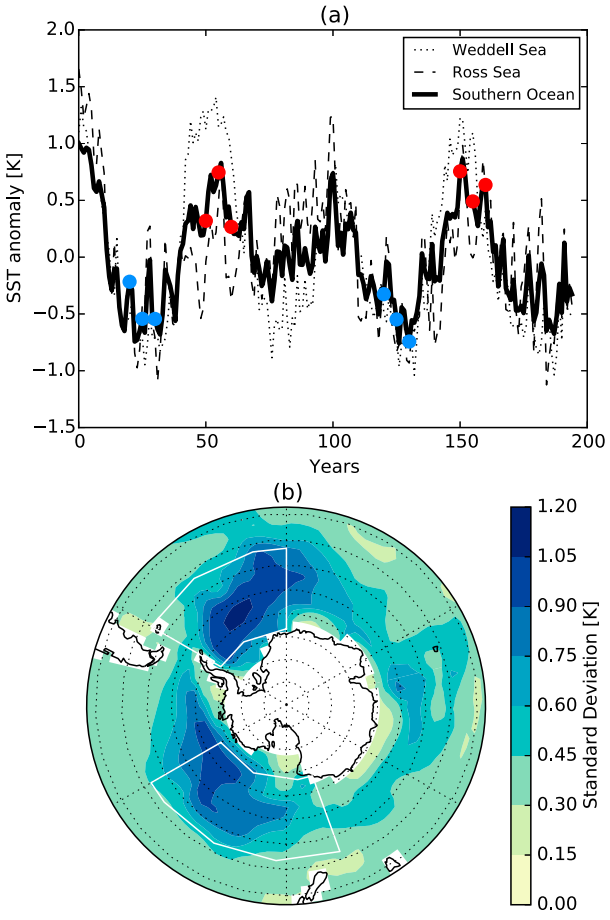

FIG. 2. (a) Annual-mean Southern Ocean (50°–70°S, solid black), Ross Sea (50°–75°S, 160°E–120°W, dashed black), and Weddell Sea (50°–75°S, 60°W–0°, dotted black) averaged SST from the pre-industrial control simulation. Red dots show the initialization dates for the warm start ozone depletion simulations, and blue dots show the cold start initialization dates. (b) Interannual standard deviation of SST from the same simulation. White trapezoidal boxes show the Ross Sea and Weddell Sea regions.

start and 6 cold start), with one daily mean ozone and one monthly mean ozone simulation initialized on each date. We begin by discussing the ensemble mean response before describing the effects of the differences in ozone forcing and the initial state.

3. Results

a. *Ensemble mean response*

Ozone depletion is seen to cause a rapid increase in zonal wind stress poleward of the climatological maximum and a small decrease equatorward of it (Fig. 3). This is indicative of a poleward shift and intensification of the extratropical jet, seen in both observations over the past few decades (Thompson and Solomon 2002)

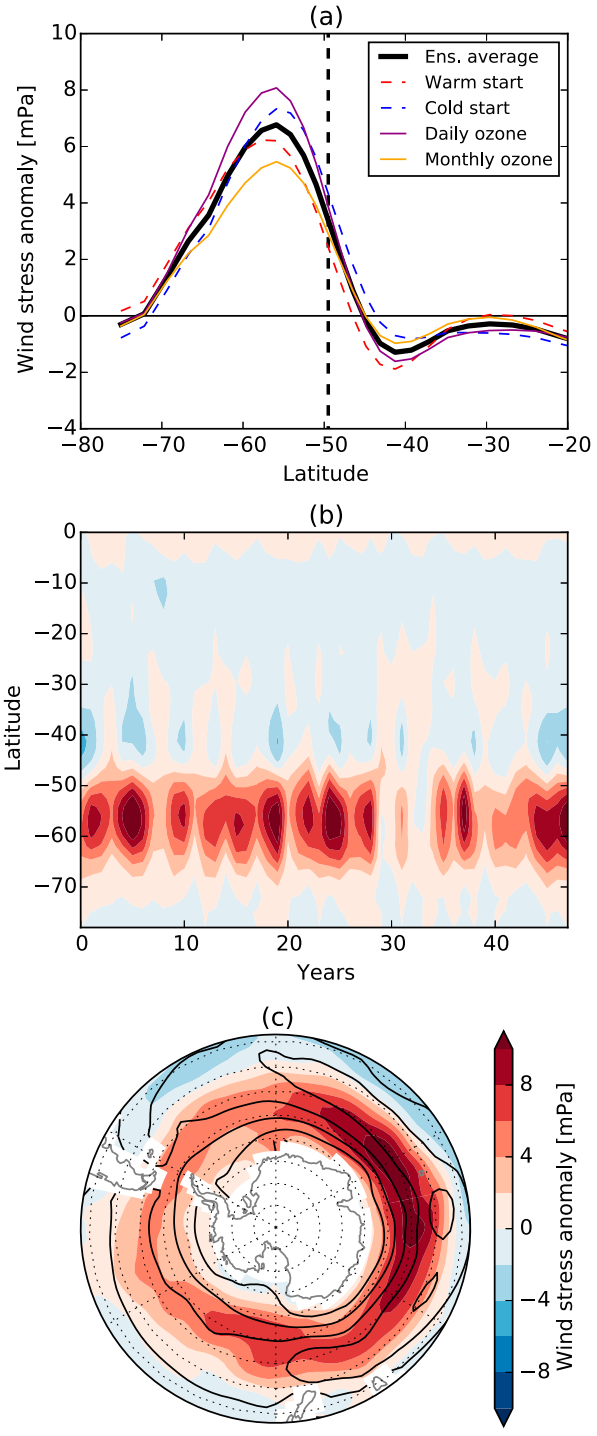

FIG. 3. (a) Annual average zonal-mean zonal wind stress anomalies, averaged over the 48 yr of the ozone perturbation simulations, for the ensemble mean (solid black), cold (blue dashed) and warm (red dashed) start ensembles, and daily (solid purple) and monthly (solid orange) mean ozone ensembles. Vertical dashed line shows the location of maximum wind stress in the control simulation. (b) Variation of zonal-mean zonal wind stress (colors) with time for the ensemble mean. (c) Zonal wind stress anomalies (colors) and climatology from the control simulation (black contours). The contour interval is 50 mPa and anomalies are calculated relative to the control simulation.

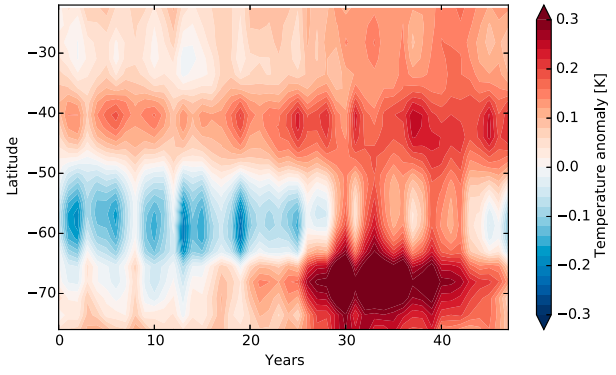

FIG. 4. Ensemble mean zonal mean SST (K) vs latitude and years. Anomalies are calculated relative to the control simulation.

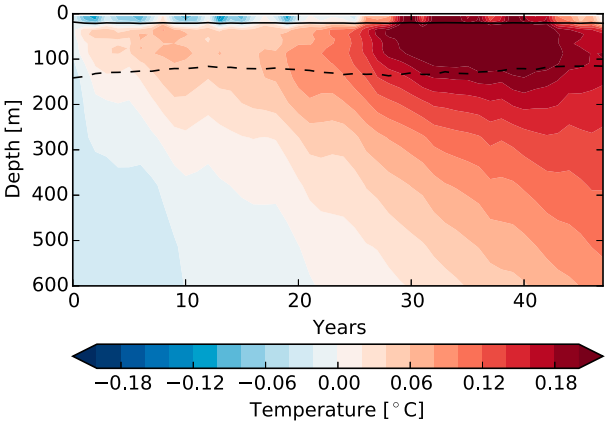

FIG. 5. Potential temperature anomaly (°C) for the ensemble mean averaged over the Southern Ocean (50°–70°S vs years. The solid and dashed black lines show the mixed layer depth, averaged over December–February and June–August, respectively.

and climate model simulations of ozone depletion (Gerber and Son 2014). The ensemble mean maximum zonal wind stress anomaly is about 7 mPa, which is less than the 12 mPa found by F15 for both the MITgcm and CCSM3.5. Although a clear increase in zonal wind stress is seen between 50° and 65°S, there is also a large amount of variability, even in the ensemble mean (Fig. 3b). This increase is also not zonally symmetric, with the largest anomalies in the Indian Ocean sector and weaker values near Western Antarctica.

This atmospheric response to ozone depletion leads to a response in the SO. Figure 4 shows the ensemble mean response of zonal mean SST following the introduction of ozone depletion. Here anomalies are calculated as the difference from the climatology of the control simulation. The initial response (years 0–25) consists of a dipole, with cooling between 50° and 70°S and warming from 50° to 35°S, a pattern which resembles the SST signature of a positive SAM on interannual time scales (Watterson 2000). After 25 yr the structure of this response changes significantly, to become a monopole, with warming present throughout the region, though it is particularly strong near the Antarctic continent (70°S). This response greatly resembles that found by F15 (see their Fig. 5) for the MITgcm, which switches from a dipole to monopole pattern after about 20 yr.

The ocean response is not limited to the surface. Figure 5 shows the ensemble mean evolution of SO temperature with depth following the introduction of ozone depletion. The initial cooling is confined near the surface, above the summer mixed layer, but a warming of the subsurface is present from the start of the simulation, growing deeper with time. The SST warming at about 25 yr occurs when this warm subsurface water is entrained into the mixed layer. The statistical significance of these temperature changes in the context of natural variability is discussed in section 3c.

The anomalous wind stress shown in Fig. 3 also drives an anomalous ocean circulation. Figure 6a shows the Eulerian meridional overturning circulation response to ozone depletion. This anomalous circulation consists of two cells that closely match the regions of positive and negative surface wind stress anomalies, with clockwise circulation from approximately 65° to 55°S and counterclockwise from 55° to 30°S. The Eulerian MOC streamlines are approximately vertical in the interior (as expected by geostrophy), with return flow in the top and bottom Ekman layers. The equatorward cell has deeper return flow, permitted by the meridional barriers in this region.

It is not the Eulerian but the residual circulation (sum of Eulerian and eddy-induced parameterized circulations) that determines the transport of heat. This residual circulation is shown alongside the Eulerian circulation in Fig. 6b. The maximum anomaly in the residual circulation at about 57°S is statistically significant from zero ($p < 0.01$ from a two-tailed t test) and is about 75% of the interannual standard deviation of the control simulation at the same location. Relative to the Eulerian circulation, the eddy-induced circulation is seen to narrow the region of anomalous upwelling (indicated by a positive meridional gradient in Ψ'_{Res}) to between approximately 67° and 57°S, as well as significantly strengthening the upwelling in this region. This strengthening may be surprising since we would expect to see some compensation between changes in the Eulerian and eddy overturning circulations (Gent 2016, and references therein). This is because an increased Eulerian overturning would be expected to tilt isopycnals further, leading to higher shear and larger Gent–McWilliams overturning. This effect is in fact seen at

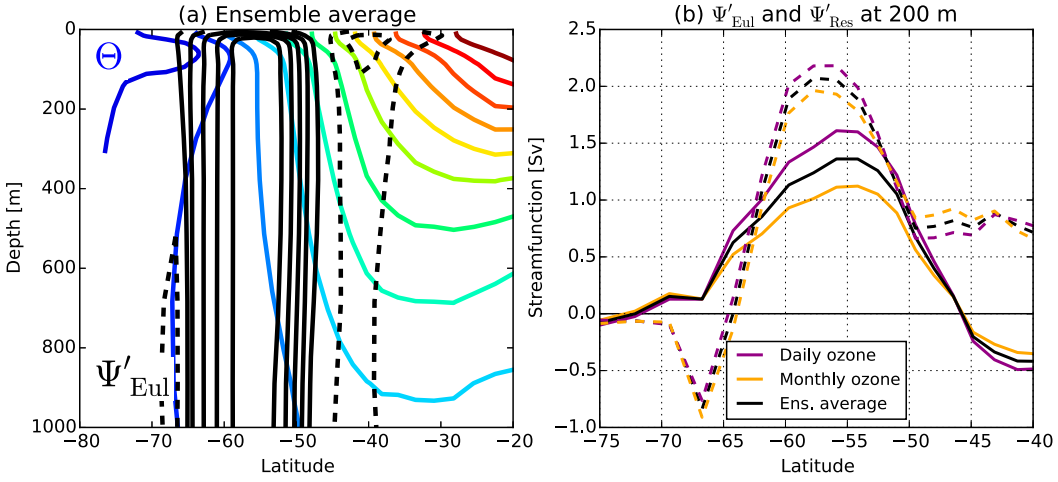

FIG. 6. (a) Ensemble average, annual-mean Eulerian MOC streamfunction vs depth and latitude response Ψ'_{EUL} (Sv; black) and potential temperature Θ (K; color). The contour interval is 2 K for temperature and 0.25 Sv for the streamfunction. Solid lines denote a clockwise circulation, dashed counterclockwise. (b) Annual-mean response of the Eulerian (Ψ'_{EUL}; solid) and residual mean (Ψ'_{Res}; dashed) MOC at 200 m, showing the ensemble average as well as daily and monthly ozone ensembles.

greater depths in the model. However, the northward motion of lighter water leads to a reduction of convection and shallower mixed layer depths. Even though there is a slight increase in the lateral density gradient, the net result is a decline in the parameterized submesoscale overturning associated with Fox-Kemper et al. (2008) that acts to reinforce the changes in wind-driven overturning. Note that only the zonal-mean circulation is analyzed here, and the circulation response may have significant zonal asymmetries, particularly given the zonally asymmetric nature of the wind stress response (Fig. 3c).

Ocean temperature increases with increasing depth below the mixed layer poleward of about 55°S (Fig. 6a) because of the presence of seasonal sea ice. The upwelling in this region is therefore expected to result in a warming. Figure 7 shows the temperature response in this upwelling region, near 62°S and 200-m depth (similar results are found at other locations in the upwelling region). Indeed, a fairly linear increase in temperature can be seen over the length of the simulation (this trend is statistically significant from zero; $p < 0.01$). The depths with the largest warming trends, from about 50 to 100 m (Fig. 5), are the same as those with the largest vertical temperature gradients (Fig. 6a), while weaker trends are seen at greater depths, where the temperature gradient is smaller. This explains the appearance of a warming growing deeper with time, shown in Fig. 5. It should be noted, however, that vertical advection is not the sole driver of this temperature trend and that vertical mixing (both eddy stirring and diapycnal mixing) also plays an important role. The magnitude of this mixing is determined by the parameterizations discussed in section 2. Can this subsurface temperature trend explain the SST warming after about 25 yr (Fig. 2)? The average initial (0–20 yr) SST response between 50° and 70°S is about −0.1 K. If these subsurface temperatures are efficiently entrained into the mixed layer, we might expect this initial cooling to be offset when subsurface anomalies reach +0.1 K. This occurs at about 21 yr (Fig. 7), so there is relatively good agreement in these time scales.

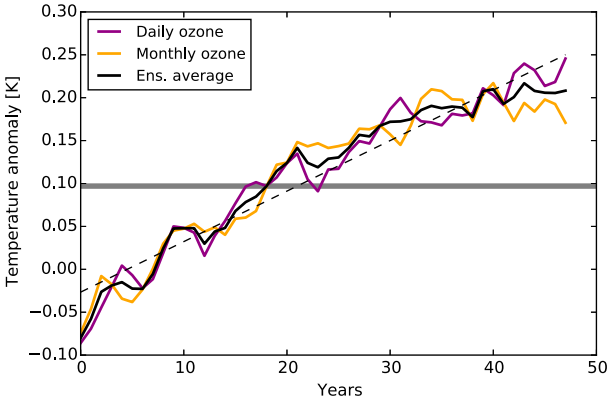

FIG. 7. Annual-mean temperature anomaly (K) at 62°S, 200 m for the daily (purple) and monthly (orange) mean ozone simulations as well as the ensemble average (black). Anomalies are calculated relative to the climatology of the control simulation. The dashed line shows the linear best fit to the ensemble average and the horizontal line represents the value of the ensemble mean SST anomaly (multiplied by −1) between 50° and 70°S over the first 20 yr.

b. *Influence of the temporal resolution of ozone forcing*

The maximum annual-mean wind stress anomaly increases by approximately 50% on changing from monthly to daily mean ozone (Fig. 3a). This difference, near the peak anomaly at 56°S, is statistically significant ($p < 0.01$) according to a two-tailed t test. In agreement with Neely et al. (2014), this indicates that linear interpolation between monthly mean values, such as was used for the majority of models that contributed to CMIP5 (Gerber and Son 2014), significantly underestimates the effects of ozone depletion.

The difference between simulations with monthly and daily mean ozone is not limited to the atmosphere. Figure 6b shows the Eulerian streamfunction at 200 m for the daily and monthly mean ozone simulations. There is an approximately 50% increase in the anomalous circulation on changing from monthly to daily mean ozone, indicating that the effect of the temporal resolution of ozone extends to the ocean interior. However, the difference between the daily and monthly mean ozone simulations is much reduced in the residual-mean circulation, indicating that parameterized eddies are acting to compensate this difference in the Ekman upwelling. Since the residual circulation determines the transport of heat, we might therefore expect similar temperature responses for the monthly and daily mean ozone simulations. Indeed, there is no significant difference in their temperature trends, as can be seen in Fig. 7.

We have seen that the differences in ozone forcing lead to a significantly different atmospheric response and Eulerian ocean circulation. However, the effect of parameterized eddies is to reduce these differences, leading to a similar subsurface temperature response. The SST responses in the daily and monthly mean ozone simulations are also similar (Fig. 8), and their differences are dwarfed by those between the warm and cold start simulations.

c. *Influence of the initial state*

The mean wind stress anomalies are similar for the cold start and warm start simulations (indeed, they are not statistically significantly different according to a two-tailed t test at any latitude), indicating that the atmospheric response is largely independent of the initial ocean state (Fig. 3a). However, Fig. 8 demonstrates the importance of the initial state in terms of the SST response; those simulations initialized with relatively warm SST cool over the first 25 yr, while those initialized with cold SST warm. Moreover, both warm and cold start simulations show reversals of these trends at around 25 yr (warm start) and 35 yr (cold start). It is not clear from Fig. 8 which part of this behavior is natural (i.e., unforced) and which, if any, is a forced response to ozone depletion. To determine this we study the difference of the ozone response simulations from the path of natural variability.

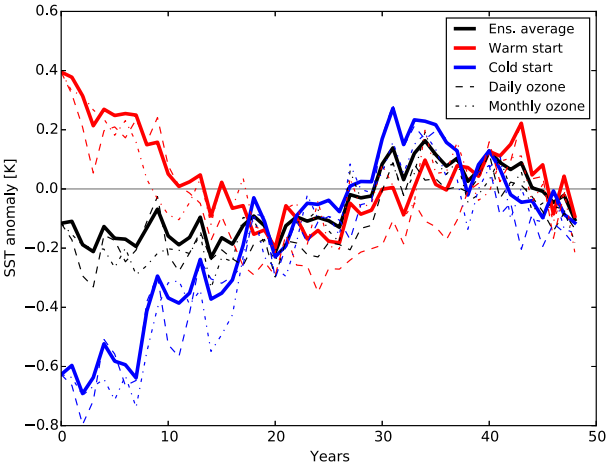

FIG. 8. Southern Ocean (50°–70°S) SST anomaly (values on y axis of −0.8 to +0.6 K) relative to the climatology of the pre-ozone depletion control simulation (solid lines for ensemble averages) and also split into daily (dashed lines) and monthly (dashed–dotted lines) mean ozone and warm (red) and cold (blue) start ensemble values. SST evolution is dominated by the initial state.

This path of natural variability could simply be taken to be that of the control simulation; however, because of the chaotic nature of SST evolution, the control simulation represents just one instance of a distribution of possible paths. Using this single control simulation path therefore introduces a large amount of noise into the results, which rapidly swamps any signal. Instead we aim to determine the path of natural variability from the autocorrelation function of SST over the 500-yr control simulation. This autocorrelation function multiplied by the initial SST then gives the expected path of natural variability of an ensemble initialized with that value. To test this method, we select from the control simulation a set of 21 yr with warm and cold SO SST, each of which must be at least one standard deviation from the mean and spaced at least 5 yr apart to mirror the initialization of the ozone response simulations. The average of the SST evolution following these years is shown as the dashed lines in Fig. 9. As well as this, the path determined by autocorrelation is shown, along with a 95% uncertainty range due to the finite length of the control simulation. The dashed lines almost always lie within the uncertainty range for the autocorrelation, showing that the autocorrelation accurately captures the unforced SST evolution.

The evolution of SST over the SO, Ross Sea, and Weddell Sea following ozone depletion for the warm

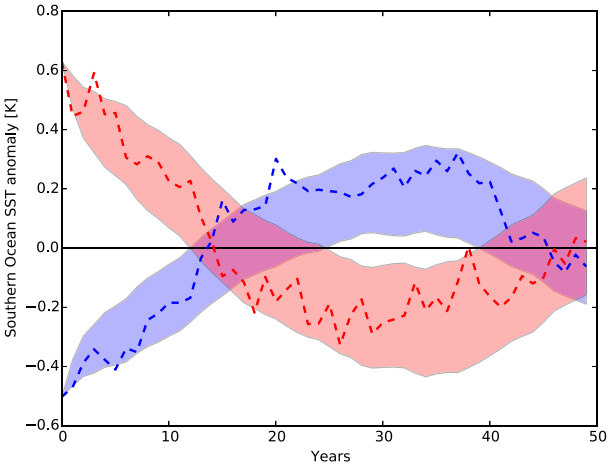

FIG. 9. Southern Ocean (50°–70°S) average SST anomaly (from values of −0.8 to +0.6 K) following 10 warm (red) and 11 cold (blue) years sampled from a 500-yr control simulation. Shaded regions represent the 95% confidence interval on the expected response calculated from the autocorrelation function. Years are selected from the control simulation, which are at least one standard deviation from the mean and spaced at least 5 yr apart in order to mirror the selection of start dates for the ozone response simulations.

and cold start ensembles is shown in Fig. 10. Also shown is the path of natural variability (Fig. 10, left) and the difference between this response and natural variability (Fig. 10, right). In the majority of cases natural variability is seen to explain the most of the SST evolution, with the SST response falling within the uncertainty range of natural variability (Fig. 10, shaded regions). A clear exception to this is the Ross Sea, particularly the warm start ensemble, which warms strongly after 15 yr, in contrast to the cooling trend of natural variability.

Differences of the forced response from natural variability (Fig. 10, right) show similar forced responses regardless of the initial conditions, although there is a large amount of variability. In almost all cases there is an initial cooling followed by a warming, with the exception of the cold start ensemble over the SO, which maintains negative anomalies throughout the length of the simulation. Interestingly, the cold start ensembles remain colder than the warm start even after the autocorrelation is removed, indicating a possible asymmetry in the responses (this result also holds pairwise, not just in the ensemble means, with 80% of all cold and warm start pairs having colder SO anomalies for the cold start simulation). These differences are, however, mostly small relative to the size of the responses. Importantly, in order to calculate the response to a time-varying forcing from the step function response it is a necessary condition that this response be independent of the initial conditions. The result that warm and cold start simulations give largely similar results therefore supports the step function response approach (Marshall et al. 2014) for predicting the response to a more realistic ozone forcing. Furthermore, the similarity of the warm and cold start ensembles (which are subsamples of the total ensemble) to the ensemble mean shows that the ensemble mean results are not highly dependent on the ensemble size.

Most of the simulations show a decrease in SST anomalies after about 40 yr. This indicates that the SO may not stabilize at a warmer temperature in our simulations, as found by F15, but rather continues to vary periodically (this periodicity is also visible in Figs. 4 and 5). The forced response may therefore be thought of as a modulation of natural variability.

Figure 10 shows some significant regional differences in the forced response to ozone depletion. First, although natural variability is larger in the Weddell Sea, the Ross Sea shows a stronger forced response, particularly in the long-term warming. Second, the time scales of the transient response are regionally dependent; the initial cooling lasts about 15 yr in the Ross Sea and about 30 yr in the Weddell Sea. These regional differences in the SST response are further illustrated in Fig. 11, which shows maps of SST anomaly over three 15-yr periods following the introduction of ozone depletion. Note that the anomalies in Fig. 11 are relative to the climatology of the pre-ozone depletion control simulation rather than the autocorrelation, which is too noisy to be used at each grid point. The Ross Sea is seen to warm in both the warm and cold start ensembles, while the Weddell Sea cools in the warm start ensemble and warms in the cold start ensemble. The net result is that the warm start ensemble results in a dipole of SST after 15 yr, while the cold start shows warming throughout the SO. In the ensemble average, the dominant long-term warming signal is seen to be in the Ross Sea.

Sea ice changes largely follow the SST patterns discussed above (Fig. 12). In the ensemble mean, there is little change in sea ice concentrations over the first 15 yr, while differences between the warm and cold start simulations are dominated by the Weddell Sea. The long-term response gives a reduction in sea ice concentrations in the Ross Sea in all cases, with opposite responses of the Weddell Sea for warm and cold start simulations and little overall change in the ensemble mean.

Changes in winter and summer sea ice area are shown in Fig. 13. In the ensemble mean, the area does not change much in either case for the first 20–25 yr but then falls to a minimum at about 30 yr, before increasing again. The peak fractional change in sea ice area is about 10% in winter and 20% during the summer, the larger fractional summer change coming at the time of the largest ozone-induced atmospheric anomalies (Thompson et al. 2011). These changes in sea ice extent are largely consistent with SO SST (Fig. 10), although there is not an initial increase

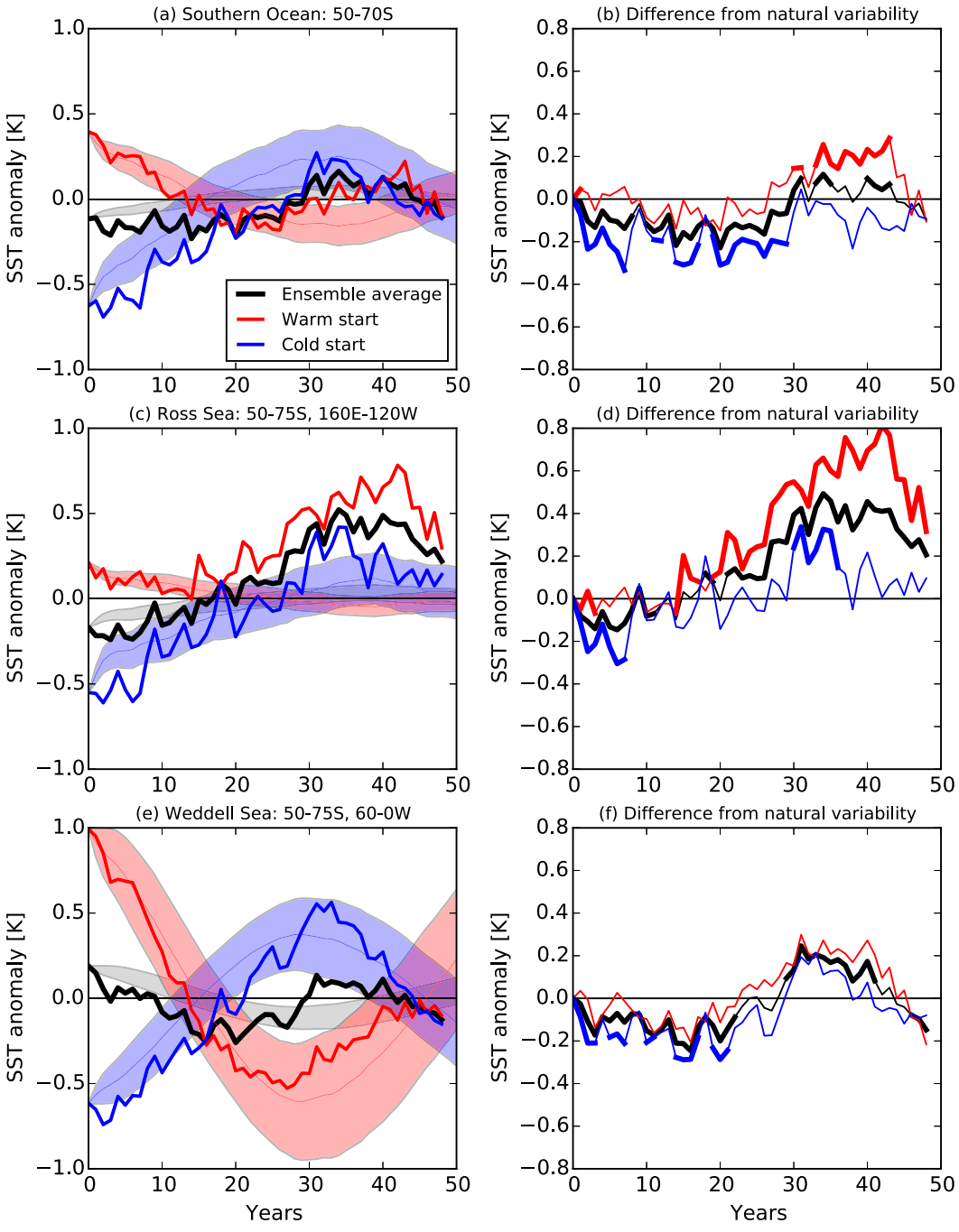

FIG. 10. (a),(c),(e) Response of Southern Ocean, Ross Sea, and Weddell Sea SST to the ozone perturbation, respectively, with the ensemble average (black) and with a warm start (red) and cold start (blue) values. Year 0 represents the initial conditions and year 1 is the first year after the perturbation is applied. The shaded region represents the 95% confidence interval on the expected response in the absence of a perturbation, calculated from the autocorrelation of a 500-yr control simulation. (b),(d),(f) As in (a),(c),(e), but for differences of the simulated response from this expected natural variability; bold lines show where this difference lies outside the interval of natural variability.

in sea ice, as might be expected from the initial cooling of SST. This may be because the largest initial SST cooling in the ensemble mean is quite far equatorward in the Ross Sea sector (Fig. 11, top left), away from the sea ice edge, and so has little effect on sea ice in this region (Fig. 12, top left). In fact, the model has a bias toward too little winter sea ice in the Ross Sea sector compared with observed values, so this SST cooling would likely have a larger effect

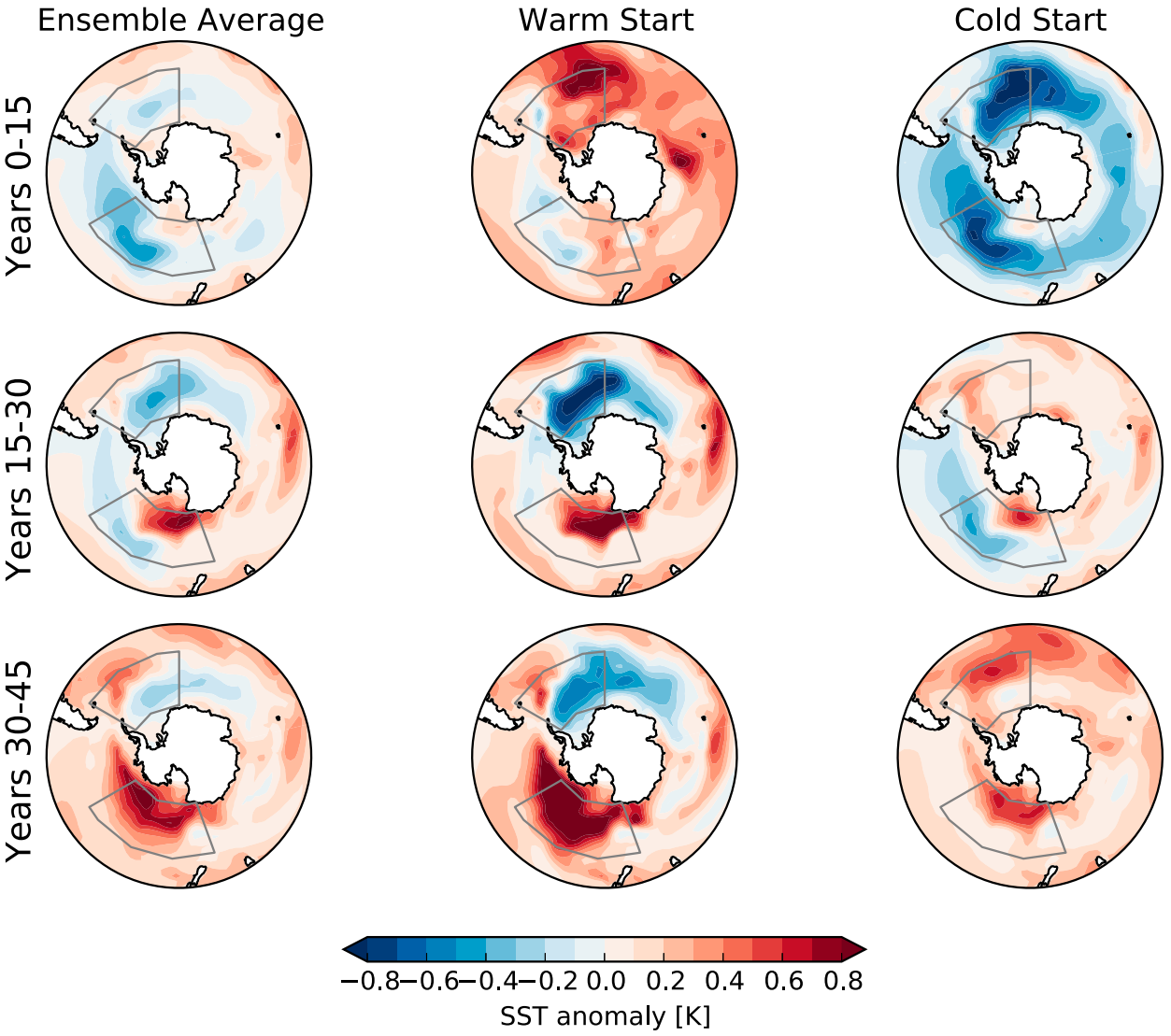

FIG. 11. SST anomaly of the ensemble mean perturbation simulations relative to the climatology of the pre-ozone depletion control simulation for (top to bottom) 0–15, 15–30, and 30–45 yr following ozone depletion and with (left to right) the ensemble average (black) and with warm start (red) and cold start (blue) values. Gray trapezoidal boxes show the Ross and Weddell Sea regions.

on sea ice under a more realistic climatology. An initial increase in winter sea ice extent might also be prevented owing to a cancellation between the effects of horizontal Ekman transport (driving a cooling) and vertical Ekman pumping (driving a warming) during this season (Purich et al. 2016), in turn resulting from seasonal changes in temperature stratification. The recovery of sea ice after 30 yr again demonstrates that the SO continues to vary periodically rather than stabilizing at a new mean value.

4. Conclusions

In this study we have investigated the transient response of the SO to a step change in stratospheric ozone depletion, using a comprehensive coupled climate model, GFDL-ESM2Mc. The main conclusions are as follows:

1) Ozone depletion causes a poleward shift of the extratropical jet, leading to enhanced zonal wind stress over much of the SO. Consistent with Neely et al. (2014), we find an approximately 50% increase in the maximum annual-mean wind stress anomaly on changing from monthly mean to daily ozone. This indicates that linear interpolation between monthly mean values, which fails to capture the sharp ozone minimum near 1 October (Fig. 1), leads to a significant underestimate of the effects of ozone depletion.

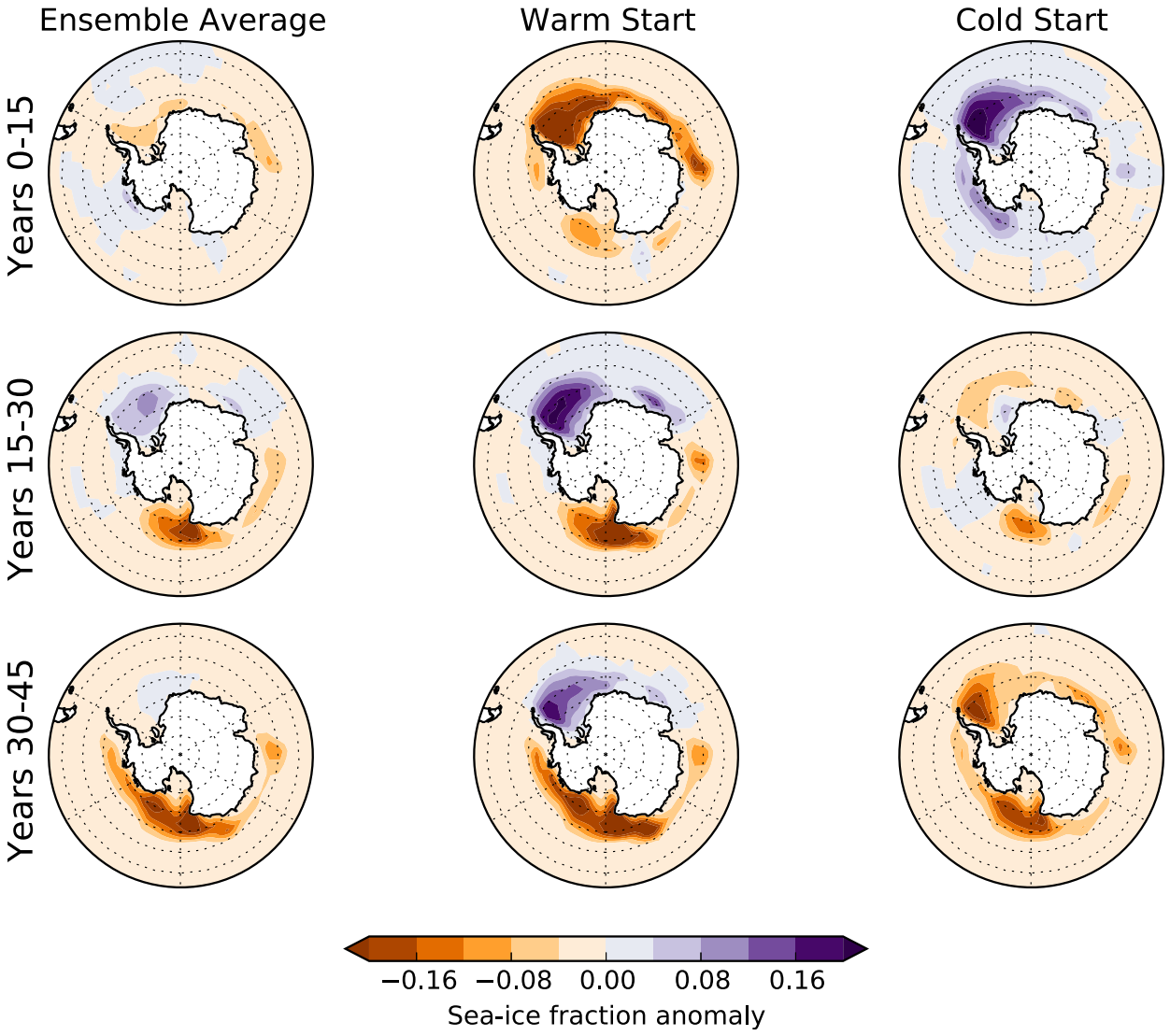

FIG. 12. As in Fig. 11, but for the winter (July–August) sea ice fraction anomaly.

The effect of the temporal resolution of prescribed ozone is not limited to the atmosphere; the stronger wind stress anomalies using daily ozone drive a stronger Eulerian MOC relative to monthly mean ozone. However, when considering the residual circulation, which includes the effect of parameterized eddies, this difference is much reduced. Since the residual circulation determines the advection of heat, there is little difference in ocean temperature between monthly mean and daily ozone simulations.

2) Following the introduction of ozone depletion, the SO SST cools and then warms after about 25 yr, similar to the result found by F15 for the MITgcm. However, in contrast to the idealized geometry setup used by F15, we are able to determine the regional responses to ozone depletion. The longest-lived initial cooling is found in the Weddell Sea, while the largest warming is in the Ross Sea. Observed SO trends over the last 30 yr have been highly regionally dependent (Parkinson and Cavalieri 2012), and this further highlights the need to study regional responses.
3) GFDL-ESM2Mc displays significant quasi-periodic natural variability, driven by SO deep convective events, which is necessary to remove in order to determine the forced response. After removing this natural variability the response is seen to be largely independent of the initial conditions (Fig. 10). This result is important because in order to construct the response to an arbitrary forcing from the step response,

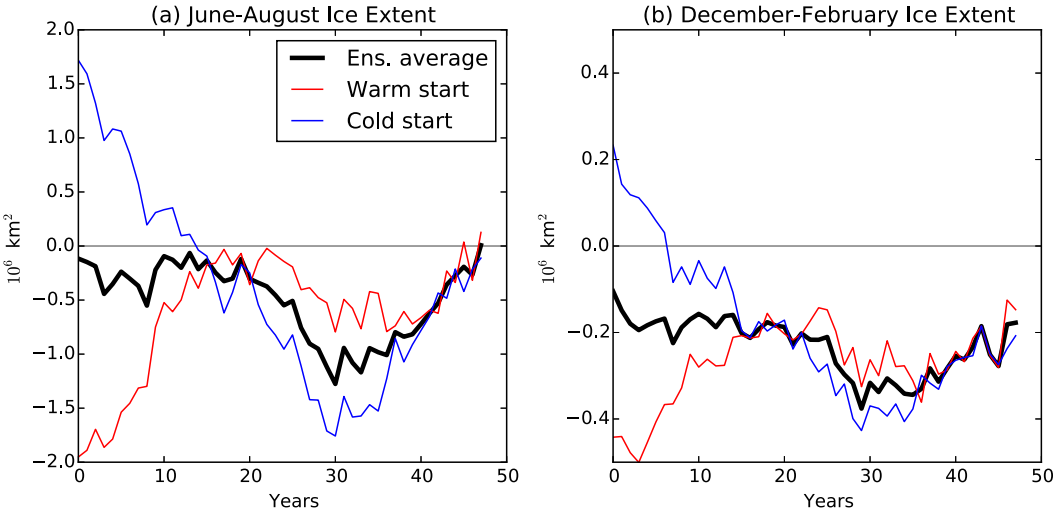

FIG. 13. Sea ice anomaly of the ensemble mean perturbation simulations relative to the pre-ozone depletion control simulation: (a) June–August and (b) December–February) with the ensemble average (black) and with the warm start (red) and cold start (blue) values. Sea ice area is calculated by summing the fraction of sea ice in each grid cell multiplied by the area of that grid cell.

it is necessary that this response be independent of the initial conditions (Marshall et al. 2014).

We have shown that wind-driven changes to the ocean residual circulation, as proposed by F15, play a significant role in driving the SO temperature response to ozone depletion. However, two further mechanisms are also important. First, changes in vertical stratification, and so convection, may be driven by both the northward Ekman transport of fresher water, as well as changes in precipitation arising from a shift in the storm tracks. Second, changes in cloud cover over the SO, again arising from a shift of the storm tracks, can significantly affect surface radiative heat fluxes (Grise et al. 2013; Solomon et al. 2015a). A detailed analysis of the relative contributions of these mechanisms will be carried out in future work.

F15 suggested that ozone depletion could have contributed to the observed expansion of sea ice cover around Antarctica in the last three decades (Parkinson and Cavalieri 2012). Indeed, given the initial 25-yr cooling seen in this study, similar to that found by F15, our results might appear to support their conclusions (although we do not find an initial increase in sea ice extent). However, it should be noted that the magnitude of the forced SO SST response found here is small compared to natural variability. The initial annual-mean SO cooling found here is about 0.1 K, but the interannual standard deviation of SO SST in GFDL-ESM2Mc is 0.4 K. Hence, it would take approximately 20 yr to detect this forced signal (at the 95% confidence level, using a two-tailed t test), which is not much less than the duration of the signal itself. This calculation only includes interannual variability, and multidecadal variability would likely make detection more difficult. Moreover, the time required to detect the response to a realistic ozone forcing rather than a step function change would be longer still. The interannual standard deviation of SO SST in the MITgcm simulation analyzed by F15 is similar to that of GFDL-ESM2Mc (D. Ferreira 2015, personal communication), though it is less periodic. The magnitude of the forced response is also similar; hence, we might expect a similar time scale to detect a signal in the MITgcm.

These results highlight the crucial role of SO natural variability in determining the detectability of ozone-depletion-driven changes. Some recent studies have found parameterized mixing to significantly affect model SO variability (Heuzé et al. 2015; Kjellsson et al. 2015), and there may be some sensitivity of the results presented here to these parameterizations. Further investigation into the factors influencing the simulation of SO variability is an important direction for future research.

Acknowledgments. This work was funded by a Frontiers of Earth System Dynamics grant from the U.S. National Science Foundation (Directorate for Geosciences FESD-1338814). We thank Doug Kinnison for providing the WACCM-SD ozone data. We made use of the Iris Python package (Met Office 2010) for data analysis and visualization. We are also grateful for the feedback of Yavor Kostov and two anonymous reviewers. Data from the simulations analyzed here are available from the authors upon request.

REFERENCES

Bitz, C. M., and L. M. Polvani, 2012: Antarctic climate response to stratospheric ozone depletion in a fine resolution ocean climate model. *Geophys. Res. Lett.*, **39**, L20705, doi:10.1029/2012GL053393.

Ciasto, L. M., and D. W. J. Thompson, 2008: Observations of large-scale ocean–atmosphere interaction in the Southern Hemisphere. *J. Climate*, **21**, 1244–1259, doi:10.1175/2007JCLI1809.1.

Cionni, I., and Coauthors, 2011: Ozone database in support of CMIP5 simulations: Results and corresponding radiative forcing. *Atmos. Chem. Phys.*, **11**, 11 267–11 292, doi:10.5194/acp-11-11267-2011.

Comiso, J. C., and F. Nishio, 2008: Trends in the sea ice cover using enhanced and compatible AMSR-E, SSM/I, and SMMR data. *J. Geophys. Res.*, **113**, C02S07, doi:10.1029/2007JC004257.

de Lavergne, C., J. B. Palter, E. D. Galbraith, R. Bernardello, and I. Marinov, 2014: Cessation of deep convection in the open Southern Ocean under anthropogenic climate change. *Nat. Climate Change*, **4**, 278–282, doi:10.1038/nclimate2132.

Dunne, J. P., and Coauthors, 2012: GFDL's ESM2 global coupled climate–carbon Earth system models. Part I: Physical formulation and baseline simulation characteristics. *J. Climate*, **25**, 6646–6665, doi:10.1175/JCLI-D-11-00560.1.

Ferreira, D., J. Marshall, C. M. Bitz, S. Solomon, and R. A. Plumb, 2015: Antarctic Ocean and sea ice response to ozone depletion: A two-time-scale problem. *J. Climate*, **28**, 1206–1226, doi:10.1175/JCLI-D-14-00313.1.

Fox-Kemper, B., R. Ferrari, and R. Hallberg, 2008: Parameterization of mixed layer eddies. Part I: Theory and diagnosis. *J. Phys. Oceanogr.*, **38**, 1145–1165, doi:10.1175/2007JPO3792.1.

Galbraith, E. D., and Coauthors, 2011: Climate variability and radiocarbon in the CM2Mc Earth system model. *J. Climate*, **24**, 4230–4254, doi:10.1175/2011JCLI3919.1.

Gent, P. R., 2016: Effects of Southern Hemisphere wind changes on the meridional overturning circulation in ocean models. *Annu. Rev. Mar. Sci.*, **8**, 79–94, doi:10.1146/annurev-marine-122414-033929.

——, and J. C. McWilliams, 1990: Isopycnal mixing in ocean circulation models. *J. Phys. Oceanogr.*, **20**, 150–155, doi:10.1175/1520-0485(1990)020<0150:IMIOCM>2.0.CO;2.

Gerber, E. P., and S.-W. Son, 2014: Quantifying the summertime response of the austral jet stream and Hadley cell to stratospheric ozone and greenhouse gases. *J. Climate*, **27**, 5538–5559, doi:10.1175/JCLI-D-13-00539.1.

Gnanadesikan, A., M.-A. Pradal, and R. Abernathey, 2015: Isopycnal mixing by mesoscale eddies significantly impacts oceanic anthropogenic carbon uptake. *Geophys. Res. Lett.*, **42**, 4249–4255, doi:10.1002/2015GL064100.

Goosse, H., W. Lefebvre, A. de Montety, E. Crespin, and A. H. Orsi, 2009: Consistent past half-century trends in the atmosphere, the sea ice and the ocean at high southern latitudes. *Climate Dyn.*, **33**, 999–1016, doi:10.1007/s00382-008-0500-9.

Grise, K. M., L. M. Polvani, G. Tselioudis, Y. Wu, and M. D. Zelinka, 2013: The ozone hole indirect effect: Cloud-radiative anomalies accompanying the poleward shift of the eddy-driven jet in the Southern Hemisphere. *Geophys. Res. Lett.*, **40**, 3688–3692, doi:10.1002/grl.50675.

Hall, A., and M. Visbeck, 2002: Synchronous variability in the Southern Hemisphere atmosphere, sea ice, and ocean resulting from the annular mode. *J. Climate*, **15**, 3043–3057, doi:10.1175/1520-0442(2002)015<3043:SVITSH>2.0.CO;2.

Hande, L. B., S. T. Siems, and M. J. Manton, 2012: Observed trends in wind speed over the Southern Ocean. *Geophys. Res. Lett.*, **39**, L11802, doi:10.1029/2012GL051734.

Heuzé, C., J. K. Ridley, D. Calvert, D. P. Stevens, and K. J. Heywood, 2015: Increasing vertical mixing to reduce Southern Ocean deep convection in NEMO3.4. *Geosci. Model Dev.*, **8**, 3119–3130, doi:10.5194/gmd-8-3119-2015.

Kjellsson, J., and Coauthors, 2015: Model sensitivity of the Weddell and Ross Seas, Antarctica, to vertical mixing and freshwater forcing. *Ocean Modell.*, **94**, 141–152, doi:10.1016/j.ocemod.2015.08.003.

Kostov, Y., J. Marshall, U. Hausmann, K. C. Armour, D. Ferreira, and M. M. Holland, 2016: Fast and slow responses of southern ocean sea surface temperature to SAM in coupled climate models. *Climate Dyn.*, doi:10.1007/s00382-016-3162-z, in press.

Large, W. G., and S. G. Yeager, 2009: The global climatology of an interannually varying air–sea flux data set. *Climate Dyn.*, **33**, 341–364, doi:10.1007/s00382-008-0441-3.

——, J. C. McWilliams, and S. C. Doney, 1994: Oceanic vertical mixing: A review and a model with a nonlocal boundary layer parameterization. *Rev. Geophys.*, **32**, 363–403, doi:10.1029/94RG01872.

Lefebvre, W., and H. Goosse, 2008: An analysis of the atmospheric processes driving the large-scale winter sea ice variability in the Southern Ocean. *J. Geophys. Res.*, **113**, C02004, doi:10.1029/2006JC004032.

——, ——, R. Timmermann, and T. Fichefet, 2004: Influence of the southern annular mode on the sea ice–ocean system. *J. Geophys. Res.*, **109**, C09005, doi:10.1029/2004JC002403.

Marshall, J., K. C. Armour, J. R. Scott, Y. Kostov, U. Hausmann, D. Ferreira, T. G. Shepherd, and C. M. Bitz, 2014: The ocean's role in polar climate change: Asymmetric arctic and Antarctic responses to greenhouse gas and ozone forcing. *Philos. Trans. Roy. Soc. London*, **372A**, 20130040, doi:10.1098/rsta.2013.0040.

Martin, T., W. Park, and M. Latif, 2013: Multi-centennial variability controlled by Southern Ocean convection in the Kiel climate model. *Climate Dyn.*, **40**, 2005–2022, doi:10.1007/s00382-012-1586-7.

Meijers, A. J. S., E. Shuckburgh, N. Bruneau, J. B. Sallee, T. J. Bracegirdle, and Z. Wang, 2012: Representation of the Antarctic Circumpolar Current in the CMIP5 climate models and future changes under warming scenarios. *J. Geophys. Res.*, **117**, C12008, doi:10.1029/2012JC008412.

Met Office, 2010: Iris: A Python library for analysing and visualising meteorological and oceanographic data sets, version 1.9. Met Office. [Available online at http://scitools.org.uk/.]

Neely, R. R., D. R. Marsh, K. L. Smith, S. M. Davis, and L. M. Polvani, 2014: Biases in Southern Hemisphere climate trends induced by coarsely specifying the temporal resolution of stratospheric ozone. *Geophys. Res. Lett.*, **41**, 8602–8610, doi:10.1002/2014GL061627.

Parkinson, C. L., and D. J. Cavalieri, 2012: Antarctic sea ice variability and trends, 1979–2010. *Cryosphere*, **6**, 871–880, doi:10.5194/tc-6-871-2012.

Polvani, L. M., D. W. Waugh, G. J. P. Correa, and S.-W. Son, 2011: Stratospheric ozone depletion: The main driver of twentieth-century atmospheric circulation changes in the Southern Hemisphere. *J. Climate*, **24**, 795–812, doi:10.1175/2010JCLI3772.1.

Pradal, M.-A., and A. Gnanadesikan, 2014: How does the Redi parameter for mesoscale mixing impact global climate in an Earth system model? *J. Adv. Model. Earth Syst.*, **6**, 586–601, doi:10.1002/2013MS000273.

Previdi, M., L. M. Polvani, and M. Previdi, 2014: Climate system response to stratospheric ozone depletion and recovery. *Quart. J. Roy. Meteor. Soc.*, **140**, 2401–2419, doi:10.1002/qj.2330.

Purich, A., W. Cai, M. H. England, and T. Cowan, 2016: Evidence for link between modelled trends in Antarctic sea ice and

underestimated westerly wind changes. *Nat. Commun.*, **7**, 10409, doi:10.1038/ncomms10409.

Redi, M., 1982: Oceanic isopycnal mixing by coordinate rotation. *J. Phys. Oceanogr.*, **12**, 1154–1158, doi:10.1175/1520-0485(1982)012<1154:OIMBCR>2.0.CO;2.

Sen Gupta, A., and M. H. England, 2006: Coupled ocean–atmosphere–ice response to variations in the southern annular mode. *J. Climate*, **19**, 4457–4486, doi:10.1175/JCLI3843.1.

Sigmond, M., and J. C. Fyfe, 2010: Has the ozone hole contributed to increased Antarctic sea ice extent? *Geophys. Res. Lett.*, **37**, L18502, doi:10.1029/2010GL044301.

——, and ——, 2014: The Antarctic sea ice response to the ozone hole in climate models. *J. Climate*, **27**, 1336–1342, doi:10.1175/JCLI-D-13-00590.1.

Smith, K. L., L. M. Polvani, and D. R. Marsh, 2012: Mitigation of 21st century Antarctic sea ice loss by stratospheric ozone recovery. *Geophys. Res. Lett.*, **39**, L20701, doi:10.1029/2012GL053325.

Solomon, A., L. M. Polvani, K. L. Smith, and R. P. Abernathey, 2015a: The impact of ozone depleting substances on the circulation, temperature, and salinity of the Southern Ocean: An attribution study with CESM1(WACCM). *Geophys. Res. Lett.*, **42**, 5547–5555, doi:10.1002/2015GL064744.

Solomon, S., D. Kinnison, J. Bandoro, and R. Garcia, 2015b: Simulation of polar ozone depletion: An update. *J. Geophys. Res. Atmos.*, **120**, 7958–7974, doi:10.1002/2015JD023365.

Swart, N. C., and J. C. Fyfe, 2012: Observed and simulated changes in the Southern Hemisphere surface westerly wind-stress. *Geophys. Res. Lett.*, **39**, 6–11, doi:10.1029/2012GL052810.

Thomas, J. L., D. Waugh, and A. Gnanadesikan, 2015: Decadal variability in the Southern Hemisphere extratropical circulation: Recent trends and natural variability. *Geophys. Res. Lett.*, **42**, 5508–5515, doi:10.1002/2015GL064521.

Thompson, D. W. J., and S. Solomon, 2002: Interpretation of recent Southern Hemisphere climate change. *Science*, **296**, 895–899, doi:10.1126/science.1069270.

——, ——, P. J. Kushner, M. H. England, K. M. Grise, and D. J. Karoly, 2011: Signatures of the Antarctic ozone hole in Southern Hemisphere surface climate change. *Nat. Geosci.*, **4**, 741–749, doi:10.1038/ngeo1296.

Turner, J., T. J. Bracegirdle, T. Phillips, G. J. Marshall, and J. S. Hosking, 2013: An initial assessment of Antarctic sea ice extent in the CMIP5 models. *J. Climate*, **26**, 1473–1484, doi:10.1175/JCLI-D-12-00068.1.

Watterson, I. G., 2000: Southern midlatitude zonal wind vacillation and its interaction with the ocean in GCM simulations. *J. Climate*, **13**, 562–578, doi:10.1175/1520-0442(2000)013<0562:SMZWVA>2.0.CO;2.

Zhang, S., M. J. Harrison, A. Rosati, and A. Wittenberg, 2007: System design and evaluation of coupled ensemble data assimilation for global oceanic climate studies. *Mon. Wea. Rev.*, **135**, 3541–3564, doi:10.1175/MWR3466.1.